Global 30–240 keV proton precipitation in the 17–18 April 2002 geomagnetic storms: 3. Impact on the ionosphere and thermosphere

Xiaohua Fang,[1] Aaron J. Ridley,[1] Michael W. Liemohn,[1] Janet U. Kozyra,[1] and David S. Evans[2]

[1] NOAA Polar Orbiting Environmental Satellites 30–240 keV proton precipitation measurements in the 17–18 April 2002 geomagnetic storms are used with a Monte Carlo ion transport model to obtain ionization and heating rates that are subsequently fed into the Global Ionosphere Thermosphere Model to investigate the proton impact on the ionosphere and thermosphere. Simulation results show that after the addition of proton precipitation in a moderate geomagnetic storm (specifically, the one during mid-April 2002), there are places at low altitudes (100–120 km) on the nightside undergoing significant increases in electron and nitric oxide (NO) densities. The enhancement can be as large as several factors or even by an order of magnitude. Moreover, the temporal profiles of the enhancement in ionospheric electron densities demonstrate a direct correlation with proton precipitation imposed on the topside boundary, and there is no integral effect. This is in contrast with a continuous buildup process illustrated in the time variation of the thermospheric NO density enhancement because NO at these altitudes has a long lifetime. In addition, by including high-energy precipitating protons in a global ionosphere thermosphere coupled model, significant changes take place in the ion convection (locally around ±20%) and in the neutral winds (locally around ±40%). This study represents the first attempt to understand the global influence of proton precipitation on the ionosphere and thermosphere using in situ observational data.

1. Introduction

[2] The ionosphere and thermosphere are overlapping, tightly coupled regions of space, and strongly affected by the near-Earth magnetospheric activity. For instance, particle precipitation from the magnetosphere at high latitudes ionizes the neutral atmosphere and thereby augments the electrical conductivity associated with the ionosphere in these regions. Ionospheric convection patterns can be largely disturbed. Thermal expansion of the atmosphere as a result of Joule heating increases neutral density at high altitudes. Ionospheric chemistry is altered by thermospheric winds and composition changes. The ionosphere-thermosphere system, however, is not a simple passive recipient of magnetospheric forcing. There are indications that the ionosphere has a direct impact on the magnetosphere through ionospheric mass outflow [cf. *Chappell et al.*,

1987; *André and Yau*, 1997, and references therein]. Ionospheric conductance can also regulate magnetosphere-ionosphere energy exchange through coupled electrodynamic processes [*Ridley et al.*, 2004a]. Therefore it is critical to understand energy and dynamics in the coupled ionosphere-thermosphere system, especially during times of high magnetospheric activity.

[3] Proton precipitation is a significant kinetic energy input to the ionosphere and thermosphere. It has been demonstrated to be one of the major sources of observed ionization enhancements [*Basu et al.*, 1987; *Senior et al.*, 1987; *Smirnova et al.*, 2004] and FUV emissions [*Frey et al.*, 2001; *Gérard et al.*, 2001]. However, little work has been done in assessing the impact of proton precipitation on the global-scale ionosphere-thermosphere system. In global models of the ionosphere and thermosphere, proton precipitation is usually neglected [*Roble and Ridley*, 1987; *Roble*, 1992; *Codrescu et al.*, 1997], or total energy fluxes are treated as if they were carried by electrons alone [*Fuller-Rowell and Evans*, 1987; *Fuller-Rowell et al.*, 1996].

[4] Recently, *Galand et al.* [1999, 2001] included proton precipitation in global ionosphere thermosphere coupled models. They compared the calculated results that included only electron precipitation to those with combined electron

[1]Space Physics Research Laboratory, University of Michigan, Ann Arbor, Michigan, USA.

[2]Space Environment Center, National Oceanic and Atmospheric Administration, Boulder, Colorado, USA.

and proton input. The simulations clearly showed that proton precipitation has a significant impact on the ionospheric and thermospheric compositions as well as on electrical conductances and neutral winds. However, a clear limitation of the analyses was that statistically constructed particle precipitation patterns were employed in their simulations. In the work of *Galand et al.* [1999], electron and proton precipitation at high latitudes was given by *Roble and Ridley* [1987]. These two types of precipitating particle populations were simply assumed to be colocated and symmetric about the magnetic noon-midnight plane. The characteristic energy of a Maxwellian distribution was assumed to vary for electrons from 1.5 keV on the dayside to 4 keV on the nightside and for protons from 3 keV to 10 keV. The global precipitation patterns in the work of *Galand et al.* [2001], on the other hand, were based upon the electron precipitation model of *Hardy et al.* [1985, 1987] and the proton precipitation model of *Hardy et al.* [1989, 1991]. A moderate level of geomagnetic activity ($Kp = 3$) was assumed in the construction of particle precipitation maps. Although the proton spectra used in the *Hardy et al.* [1989, 1991] models were extrapolated from 30 keV up to 100 keV, the extrapolation to high energies was premised on the assumption of a Maxwellian distribution. The high-energy tail [e.g., *Lyons and Evans*, 1984] was thus underestimated.

[5] In this paper the global impact of proton precipitation on the ionosphere and thermosphere is analyzed using more realistic conditions. The April 2002 storms are selected in this work, as they contain a rich spectrum of geophysical phenomena, including a sheath driven storm, a magnetic cloud driven storm and global sawtooth oscillations [*Liemohn et al.*, 2004, 2005; *Clauer et al.*, 2006; *Henderson et al.*, 2006]. The availability of global in situ measurements from National Oceanic and Atmospheric Administration (NOAA) Polar Orbiting Environmental Satellites (POES) provides a unique opportunity to investigate the contributions of ion precipitation to the ionsphere and thermosphere.

[6] This study is the third one in a series of papers dedicated to the investigation of energetic proton precipitation during the 17–18 April 2002 geomagnetic storms. In the first companion paper [*Fang et al.*, 2007a, hereinafter referred to as paper 1], global 30–240 keV proton precipitation patterns during the storms were constructed using recently developed 3-hour NOAA/POES data products. The proton precipitation pattern change was shown to be highly statistically correlated with the variation of other geophysical indices, justifying the selection of a 3-hour time window for the creation of the global energetic proton precipitation maps. In the second companion paper [*Fang et al.*, 2007b, hereinafter referred to as paper 2], the constructed energetic proton precipitation patterns were employed as the energy input to drive a three-dimensional (3-D) Monte Carlo ion transport model [*Fang et al.*, 2004]. It was found that with the neglect of the beam spreading effect [*Fang et al.*, 2004, 2005, and references therein], a moderate overestimation (up to 10%) in the Pedersen and Hall conductances occurs at the center of the major proton precipitation region, while a severe underestimation (around −50% or worse) is induced along the edge (particularly along the equatorward edge). This first assessment of the horizontal spreading effect on the conductances leads to the

conclusion that 3-D particle scattering is important and needs to be included in a global model. In the present study the ionization and heating generated by precipitating energetic protons (with the beam spreading considered) are fed into an ionosphere thermosphere coupled model to assess the global impact. The current paper presents an improvement over previous studies [e.g., *Galand et al.*, 1999, 2001] in three aspects.

[7] First of all, rather than relying on statistical maps, 3-hour observational data sets for particle precipitation during the April 2002 geomagnetic storm events are used. Given that the in situ proton measurements have spectral information, the approximation of a Maxwellian energy distribution is not necessary any more. Precipitating protons are discriminated into 31 energy bands to cover the range of 30–240 keV. In addition, more realistic high-latitude electron precipitation is included using results from the assimilative mapping of ionospheric electrodynamics (AMIE) technique [*Richmond and Kamide*, 1988; *Richmond*, 1992].

[8] Second, the horizontal spreading effect is estimated and included using our 3-D Monte Carlo ion transport model [*Fang et al.*, 2004]. Charge exchange collisions between incident ions and the atmosphere result in hot neutral atoms, which can freely move across magnetic field lines until they are converted back into ions through electron stripping collisions. Proton and hydrogen atom transport are coupled together so that an incoming proton beam is not bound to the local magnetic field line but diffuses over a wider region during the transport, and the intensity is reduced at the beam center. The spatial spreading effect adds a complexity to the ion precipitation. It has been illustrated that a significant error in the localized ionization rates can stem from the omission of the spatial spreading [e.g., *Fang et al.*, 2005]. However, this effect cannot be taken into account in previous studies in which 1-D ion transport calculation was employed, such as those of *Galand et al.* [1999, 2001].

[9] Third, unlike using statistical particle precipitation patterns, the temporal variation of particle energy input and the consequent effects on the ionosphere-thermosphere system can be analyzed for different storm phases. The maps at a 3-hour cadence provide new information on the development and variability of the structure in the global high-energy ion precipitation as well as atmospheric geoeffectiveness. While this rate is not sufficient to resolve rapid precipitation variations, it is the best rate possible with NOAA's present fleet of satellites, and it is fast enough to resolve large-scale changes in the precipitation within each storm phase.

2. Global Ionosphere-Thermosphere Model (GITM)

[10] GITM is a time-dependent first-principles 3-D coupled ionosphere thermosphere model extending from 95 km to 500+ km altitude, which has been newly developed at the University of Michigan [*Ridley et al.*, 2004b, 2006]. It self-consistently solves the continuity, momentum, and temperature equations for the thermospheric neutrals and the ionospheric plasma. The ion momentum equation is solved under the assumption of steady state, taking into account the
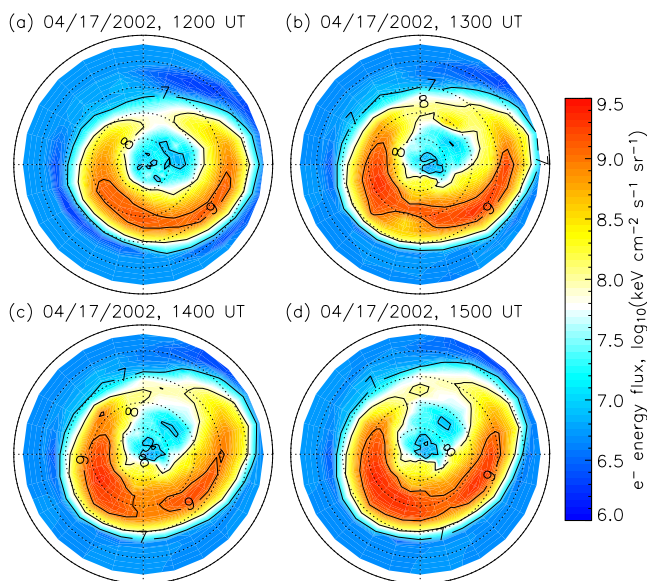
Figure 1. Snapshots of precipitating electron energy fluxes (spaced 1 hour apart) during the time interval of 1200–1500 UT on 17 April 2002. The values are shown on a logarithmic scale with contours every decade. The view is over the geographic north pole with local noon to the top and dawn to the right. The perimeter latitude is 40° and the dashed circles are 10° apart.

neutral winds and external electric field in addition to thermal pressure and gravity. The electron movement is controlled by the $\mathbf{E} \times \mathbf{B}$ drift. In the model, the vertical and horizontal neutral advections are separately solved. In the vertical direction, each neutral constituent has a separate velocity with coupling of the velocities through neutral-neutral and ion-neutral friction. A key distinguishing feature of GITM as compared to other general circulation models is that the assumption of hydrostatic equilibrium is removed. Furthermore, an altitude grid is used rather than a pressure-based coordinate system, as in other global ionosphere thermosphere coupled models. In the horizontal direction, all of the neutral species are assumed to move with the same velocity.

[11] In the GITM model the high-latitude dynamics is specified by the input from external models. At high latitudes, ion production rates due to auroral electron precipitation are specified by *Frahm et al.* [1997], given an incident Maxwellian distribution with a specified average energy and total energy flux. It is worth noting that GITM does not include a mapped dynamo electric field at low latitudes and therefore neglects the equatorial fountain effect in the present version.

3. Results

[12] Paper 1 represents the first attempt of constructing global energetic proton precipitation maps at a reasonable cadence using in situ satellite observations. In paper 2 these maps are applied as a topside energy input to a 3-D Monte Carlo ion transport model [*Fang et al.*, 2004] to simulate the interaction with the upper atmosphere. It is found that proton precipitation as well as its associated horizontal

spreading effect are important and need to be included in any global Pedersen and Hall conductance model. In this paper, the 3-D interaction results (that is, the spreading effect is considered) are added as inputs to the GITM model to assess the proton impact on the ionosphere and thermosphere system.

[13] It is easy to include proton precipitation in GITM, although auroral electrons are the only kinetic energy input at high latitudes that is routinely represented in the model. The coupling between proton precipitation and the ionosphere and thermosphere is achieved by including the resulting ionization rates in the continuity equations of O^+, N_2^+, and O_2^+, and adding the heating rates to the source terms in the neutral temperature equation. The heating of electrons and ions by energetic proton input is neglected. The grid spacing is 2.5° geographic latitude by 5° geographic longitude for the simulations reported here. The altitude spacing is specified to be approximately 0.3 of a scale height on the dayside. It is then applied everywhere and is kept static during the model run. The temporal resolution is around 2 s, limited by the explicit time-stepping advection solver in GITM.

[14] Like papers 1 and 2, three representative 3-hour proton precipitation patterns are selected and separately studied in GITM for the April 2002 storms, starting from (1) 16 April, 1200 UT (for a prestorm condition); (2) 17 April, 1200 UT (for a sheath driven storm); and (3) 18 April, 0300 UT (for a magnetic cloud driven storm). For each of them, we perform a separate model run, beginning on 15 April, 0000 UT. The atmospheric and ionospheric conditions are initiated using the MSIS-90 [*Hedin*, 1991] and IRI [*Rawer et al.*, 1978; *Bilitza*, 2001] models, respectively. The initial ionospheric convection in the first 24 hours is driven by the *Weimer* [1996] electric potential patterns. The AMIE technique [*Richmond and Kamide*, 1988; *Richmond*, 1992] is used to derive high-latitude electron input and electric fields afterward.

[15] In this study, we run quantitative comparisons between two cases. In case one, only electron precipitation is considered. In case two, in addition to auroral electrons (which have exactly the same patterns as those in case one), proton precipitation is included but limited to one of the 3-hour intervals: (1) 16 April, 1200–1500 UT, (2) 17 April, 1200–1500 UT, and (3) 18 April, 0300–0600 UT. That is, the simulation conditions are identical except for the addition of a 3-hour time window of proton precipitation in case two. By comparing the two cases that are running for different storm phases, we can quantitatively investigate the proton contributions to the ionosphere-thermosphere system at different levels of magnetospheric activity. Note that for these model runs, electron precipitation patterns are derived from IMAGE/FUV measurements [*Mende et al.*, 2000] incorporated into the AMIE technique and thus are more realistic and time-varying. The electron precipitation pattern is changed every 60 s in GITM. Figure 1 presents a series of snapshots of precipitating electron energy fluxes every 1 hour during 1200–1500 UT on 17 April 2002. In contrast with frequently varying electron precipitation, proton precipitation patterns change much more slowly at a 3-hour cadence in keeping with ring current decay timescales. In this paper, the proton precipitation patterns
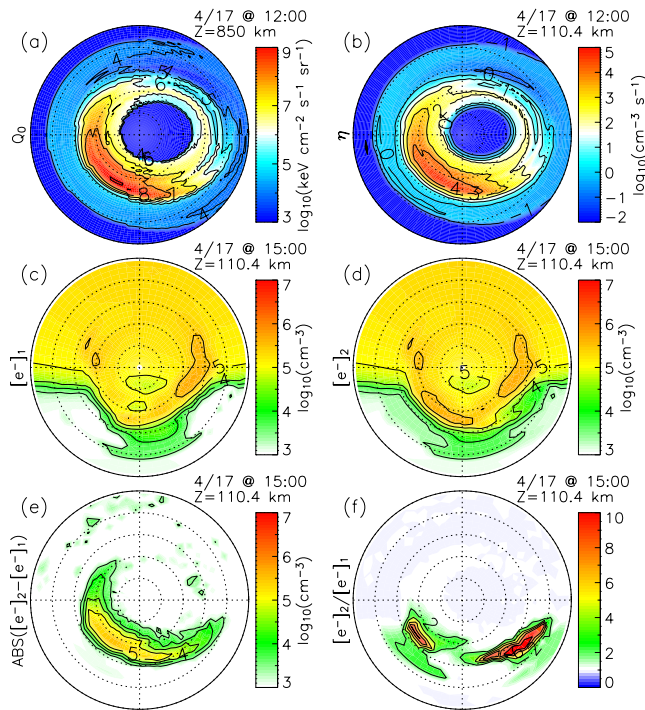
Figure 2. Proton precipitation conditions in the Global Ionosphere Thermosphere Model (GITM) simulation (case two, combined electron and proton precipitation) and comparison of ionospheric electron densities between case one (only electron precipitation) and case two. Shown here is (a) incident NOAA Polar Orbiting Environmental Satellites (POES) $30-240$ keV proton energy fluxes at 1200 UT on 17 April at 850 km altitude, (b) proton generated ionization rates at 110.4 km altitude, (c) GITM calculated ionospheric electron densities at 110.4 km 3 hours later in the simulation case one, (d) GITM calculated electron densities in case two, when additional proton precipitation is included during $1200-1500$ UT on 17 April, (e) absolute difference of the electron densities between the two cases, and (f) their ratios. All the plots (except Figure 2f) are on a logarithmic scale. The view is over the geographic north pole with local noon to the top and dawn to the right. The perimeter latitude is $40°$.

are held fixed in both time (during the 3-hour interval of the data) and space (with respect to geographic local time). By subtracting the simulation results in case one from those we get in case two, we will assess the net effect of the impact of protons on the ionosphere and thermosphere based on storm time global particle precipitation measurements.

3.1. Detailed Examination for 1200 UT on 17 April 2002

[16] As an example, Figure 2 shows the comparison of the ionospheric electron densities between the two GITM simulation cases, in the absence or presence of $30-240$ keV proton precipitation during $1200-1500$ UT on 17 April. The altitude of 110.4 km (E region), which is approximately the altitude of peak energy dissipation by incident protons (see

paper 2), is selected for this comparison. The comparison between the two simulation cases is made at the end of the 3-hour interval. The results at other altitudes and in the course of the 3-hour time window will be shown later. For convenience, the precipitating proton energy flux at 850 km altitude (case two) is reproduced in Figure 2a. The resulting ionization rates at 110.4 km altitude from incident protons are also repeated in Figure 2b, similar to what presented in paper 2 but at a slightly different altitude.

[17] Ionospheric electron densities [e$^-$] in Figure 2c and Figure 2d demonstrate the relative contribution of the solar extreme ultraviolet radiation and high-latitude particle input. The solar radiation dominates the dayside ionosphere, while on the night side auroral particle precipitation maintains the polar ionosphere. It is worth pointing out that electron produced ionization (in both Figure 2c and Figure 2d) is derived using the GITM neutral density profiles, while proton produced ionization (in Figure 2d) is obtained using the MSIS-90 atmosphere model [*Hedin*, 1991] and is subsequently fed into the GITM model. The lack of a self-consistent addition of proton precipitation in GITM is due to the fact that very long computational time is needed to run the 3-D Monte Carlo ion transport model [*Fang et al.*, 2004]. However, this simplification is not inappropriate for two reasons. First, the MSIS and GITM atmospheres actually are relatively close to each other [*Ridley et al.*, 2006]. Second, this study aims to provide a general impression of how important proton precipitation is by using more realistic particle input conditions in the global ionosphere-thermosphere modeling. It is of interest in future studies to self-consistently include the 3-D results of proton precipitation in a global model.

[18] Figure 2e shows the comparison between the simulation case one (for only electron input) and case two (for combined electron and proton input), clearly illustrating the significance of including $30-240$ keV proton precipitation in the ionosphere modeling. Note that the subscript number "1" ("2") denotes a simulation case in which $30-240$ keV proton precipitation is excluded (included). As seen in Figure 2e, precipitating protons can strongly contribute to the electron concentration, with a peak increase (over electron input only) of 3.1×10^5 cm^{-3} at $66.25°$N and 2150 LT. The longitudinal and latitudinal range for the net increase is consistent with the area in which incident protons produce significant ionization (Figure 2b). However, the locations that have maximum values do not overlap exactly with each other.

[19] Figure 2f explicitly presents the relative significance of high-energy protons by taking the ratio of the electron concentrations, [e$^-$]$_2$/[e$^-$]$_1$. The green-red shading represents a substantial increase by more than a factor of 2. It is seen that proton impact can greatly enhance ionospheric electron densities by locally up to more than an order of magnitude. Note that the maximum relative enhancement does not occur at the same region as the maximum net increase. However, there are significant regions where proton precipitation creates a substantial net increase in the electron concentration both in magnitude and in percent change. As a consequence, a severe underestimation can be made by simply considering electrons as the only particle ionization source to the ionosphere.
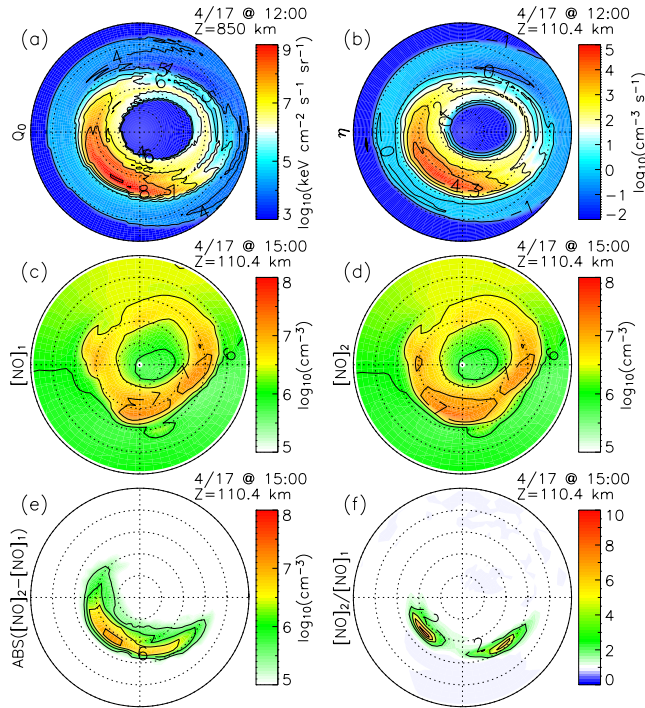
Figure 3. Similar to Figure 2 but for the comparison of thermospheric nitric oxide densities between the two GITM simulation cases, in the absence or presence of energetic proton precipitation. For the comparison purpose, Figure 2a and Figure 2b are repeated here.

[20] It is clear in Figure 2f that the relative increase of electron densities breaks into two peaks. One is located premidnight (63.75°N, 1950 LT) with a maximum ratio of $[e^-]_2/[e^-]_1 = 14.8$. It should be emphasized that this place does not coincide with the region of maximum net increase but is actually displaced equatorward of it. This offset is reflective of the fact that the low-latitude boundary of proton precipitation is equatorward of the electron precipitation boundary in the dusk sector [*Hardy et al.*, 1989]. The other peak is in the postmidnight sector (56.25°N, 0330 LT) and has a maximum ratio of 36.2. However, the net increase of electron densities is actually moderate in the early morning hours. At latitudes equatorward of the two peaks, the relative enhancement is still considerable, although the absolute difference may not be important. Another feature evident in Figure 2f is that the relative contribution of proton precipitation to ionospheric electron densities is modest at midnight, despite the large ionization enhancement. This is because the location of electron precipitation coincides with that of protons at midnight, but the electrons carry comparable or larger energy flux (see Figure 1). This is consistent with statistical findings by *Hardy et al.* [1989]. In addition, we see that the proton impact in the late afternoon sector is overwhelmed by the photoionization, in spite of considerable ionization.

[21] Particle precipitation can also have a significant effect on the thermosphere. For this study, impacts on the thermosphere are measured by changes in nitric oxide (NO) densities. NO is a minor but important atmospheric constituent in the thermosphere, and it has been the subject of

considerable interest in scientific research because of its important role in the atmospheric physics and chemistry [e.g., *Barth*, 1992; *Baker et al.*, 2001]. Because of a low ionization potential (9.25 eV), charge transfer occurs relatively easily in collisions between NO and the ions produced by photoionization and particle impact ionization. NO thus has an important effect on the ion composition in the ionospheric E region. Through radiative cooling by 5.3 μm emission, NO affects the temperature structure of the ionosphere and thermosphere in the altitude region of 120–200 km. In addition, NO has a long lifetime, particularly during the winter, so it can be transported downward from the lower thermosphere to the stratosphere [*Barth et al.*, 1999; *Callis et al.*, 1998]. Therefore it can have a significant effect on the depletion of the ozone (O_3) layer. In the chemical reactions attributed to the O_3 catalytic destruction, O_3 is destroyed but NO is regenerated [e.g., *Taylor*, 1991]. This catalytic cycle is one of the most important processes that affect the balance between O_3 creation and destruction. In this work we investigate how energetic proton precipitation influences the NO concentration and therefore the thermosphere.

[22] It has been well established in past studies that the nitric oxide concentration in the high-latitude thermosphere is controlled by particle precipitation [*Gérard and Barth*, 1977; *Siskind et al.*, 1989]. Ionization is significantly enhanced due to auroral particle bombardment. The reactions of the ionized particles N_2^+, N^+, O_2^+, and O^+ together with O, O_2, N, and N_2, respectively, account for the increase of NO^+. The dissociative recombinations of NO^+ and N_2^+ lead to the production of excited atomic nitrogen, $N(^2D)$ [*Barth*, 1992; *Bailey et al.*, 2002]:
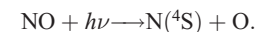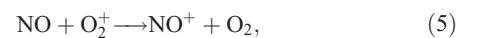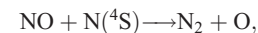
$$NO^+ + e^- \longrightarrow N(^2D,^4S) + O, \tag{1}$$

$$N_2^+ + e^- \longrightarrow 2N(^2D,^4S). \tag{2}$$
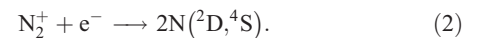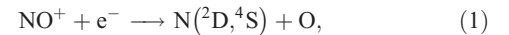
Excited atomic nitrogen is the primary production source of NO below 120 km altitude,

$$N(^2D) + O_2 \longrightarrow NO + O. \tag{3}$$
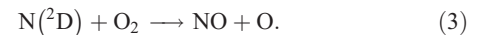
Ground state atomic nitrogen provides the production of NO at higher altitudes,

$$N(^4S) + O_2 \longrightarrow NO + O. \tag{4}$$
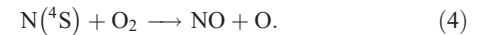
NO is lost mainly by the reactions with ground state atomic nitrogen and O_2^+ as well as photodissociation:

$$NO + N(^4S) \longrightarrow N_2 + O,$$
$$NO + O_2^+ \longrightarrow NO^+ + O_2, \tag{5}$$
$$NO + h\nu \longrightarrow N(^4S) + O.$$

[23] Similar to Figure 2, Figure 3 presents for comparison the NO densities in two simulation cases: without ($[NO]_1$) or with ($[NO]_2$) the inclusion of proton precipitation in

GITM. Again, it is clearly demonstrated that the presence of proton input can significantly contribute to the ionization, and as a consequence, the net increase of the nitric oxide. Figure 3e shows that in general this enhancement is colocated with the region of high proton ionization (Figure 3b). The net NO increase has a peak value of 1.2×10^7 cm^{-3} at 66.25°N and 2150 LT, the same place as for the maximum electron density increase (Figure 2e). Similar to electron densities, the relative increase of the nitric oxide displays a double-peak structure: one is located in the premidnight sector (66.25°N, 2110 LT) with a maximum ratio of [NO]$_2$/[NO]$_1$ = 9.0, while the other is at postmidnight (61.25°N, 0250 LT) and has a peak value of 7.1. Again, these peak relative enhancements do not occur at the same place as the net maximum NO increase. The relative increase of NO is not as large as that of the electron density, however, regions of very dramatic change (both in magnitude and in percent) exist.

[24] It is difficult to make a direct quantitative comparison of our results with *Galand et al.* [1999, 2001], since the models and the input parameters are quite different. In addition, the simulations presented here are performed under more realistic incident conditions of electrons and protons, rather than using statistical particle precipitation patterns. Moreover, this study is focused on a higher-energy component for protons, that is, 30–240 keV. The chosen energy range includes the bulk of the ring current, while a lower energy range is dominated by plasma sheet precipitation. Because the statistical proton models used in the work of *Galand et al.* [1999, 2001] include only auroral proton energies in moderately disturbed conditions ($Kp = 3$), the significance of including proton input in a global ionosphere thermosphere coupled model may be underestimated in their studies. The results presented here show that in a moderate geomagnetic storm, like the one during April 2002, at some places, protons can contribute to a large increase of electron and NO densities.

3.2. Temporal Development of the Influence of Proton Precipitation

[25] Unlike the previous studies of *Galand et al.* [1999, 2001], in which the proton effect on the ionosphere and thermosphere was investigated after a more than 1-day simulation, this paper examines the relative impact of proton precipitation and also follows the temporal evolution during a 3-hour period.

[26] Figure 4 shows the comparison of ionospheric electron densities and their temporal evolution by presenting results 10 min, 1 hour, and 3 hours after including proton precipitation during a storm phase, which starts from 1200 UT on 17 April 2002. As mentioned before, it is representative of the proton precipitation condition when the shocked solar wind hit the Earth's magnetosphere. It is worth emphasizing that electron precipitation conditions are changed every 60 s (see Figure 1), derived using the AMIE technique [*Richmond and Kamide*, 1988; *Richmond*, 1992], while the proton precipitation pattern during a 3-hour simulation time period is fixed.

[27] Figure 4 shows that as intense proton precipitation occurs during 17 April, the significance of proton impact on the ionosphere is evidently clear. In accordance with the ionization from incident protons, a large net increase of

electron densities is observed over the altitude range of 100–200 km. There are places at low altitudes (100–120 km), where protons are a dominant source of ionization and therefore can exclusively account for the electron concentration. A notable feature of the proton impact on the ionosphere is that, in general, the enhancement of electron densities illustrates a direct correlation with proton precipitation (compare Figure 4 with Figure 2a and Figure 2b), and there is no clear trend observed with time. This conclusion is supported by Figure 5, which shows the time variation of the maximum increase of electron densities at four altitudes (100.0 km, 110.4 km, 120.0 km, and 203.8 km). In addition to the change associated with the sheath driven storm phase, the temporal variations of the electron density enhancements during a quiet time period (1200–1500 UT on 16 April) and a magnetic cloud driven storm phase (0300–0600 UT on 18 April) are also included. The quantitative comparison in Figure 5 confirms that there is no clear increasing or decreasing pattern over time. The rise time of the electron density enhancement from zero to a steady value is well within 10 min for all of the curves in Figure 5 because of a very short timescale (<10 min) for the electron recombination loss. Moreover, it is shown that the maximum impact on the ionosphere of including energetic proton precipitation occurs at about 110 km altitude, where the particle ionization rate peaks for >30 keV protons.

[28] A striking feature displayed in Figure 4 is the considerable electron density decline at ∼200 km altitude, after including proton precipitation in GITM for 3 hours (the blue patch in the lower right plot of Figure 4). The region of decrease is located equatorward of the main proton precipitation (<60°) in the evening sector. This can be interpreted as a consequence of the change in the vertical ion convection. Figure 6 demonstrates how the inclusion of proton precipitation affects the vertical ion velocity at different altitude levels. It is seen that the decrease of the downward ion speed at 203.8 km altitude (the yellow and red shading in the evening sector of the top right plot in Figure 6) is coincident with the electron density depletion. Also note that the electron concentration increases with increasing altitude in this same region (compare the shading in the two lower left plots in Figure 4). The net effect is that the downward electron transport effect is weakened, resulting in a relative density depletion at this location. It should be mentioned that the comparison between Figures 4 and 6 suggests that plasma transportation is a plausible explanation to account for the localized electron density decrease. A comprehensive examination of other processes (for example, chemical reactions) is far beyond the scope of this paper and thus will not be discussed here.

[29] It is found that the significance of proton impact on the ionosphere is not as global as expected for the sawtooth oscillations on 18 April (not shown here). The sawtooth oscillations on 18 April have a very large MLT extent to their dispersionless injection region at geosynchronous orbit [*Henderson et al.*, 2006] and a very large extent to their dipolarization signatures in ground-based magnetometer perturbations [*Clauer et al.*, 2006]. However, the significance of including protons in a global model is mostly limited in the dusk-midnight quadrant. This happens for two reasons. First, during this time period, the displacement of the geomagnetic north pole from the geographic north pole
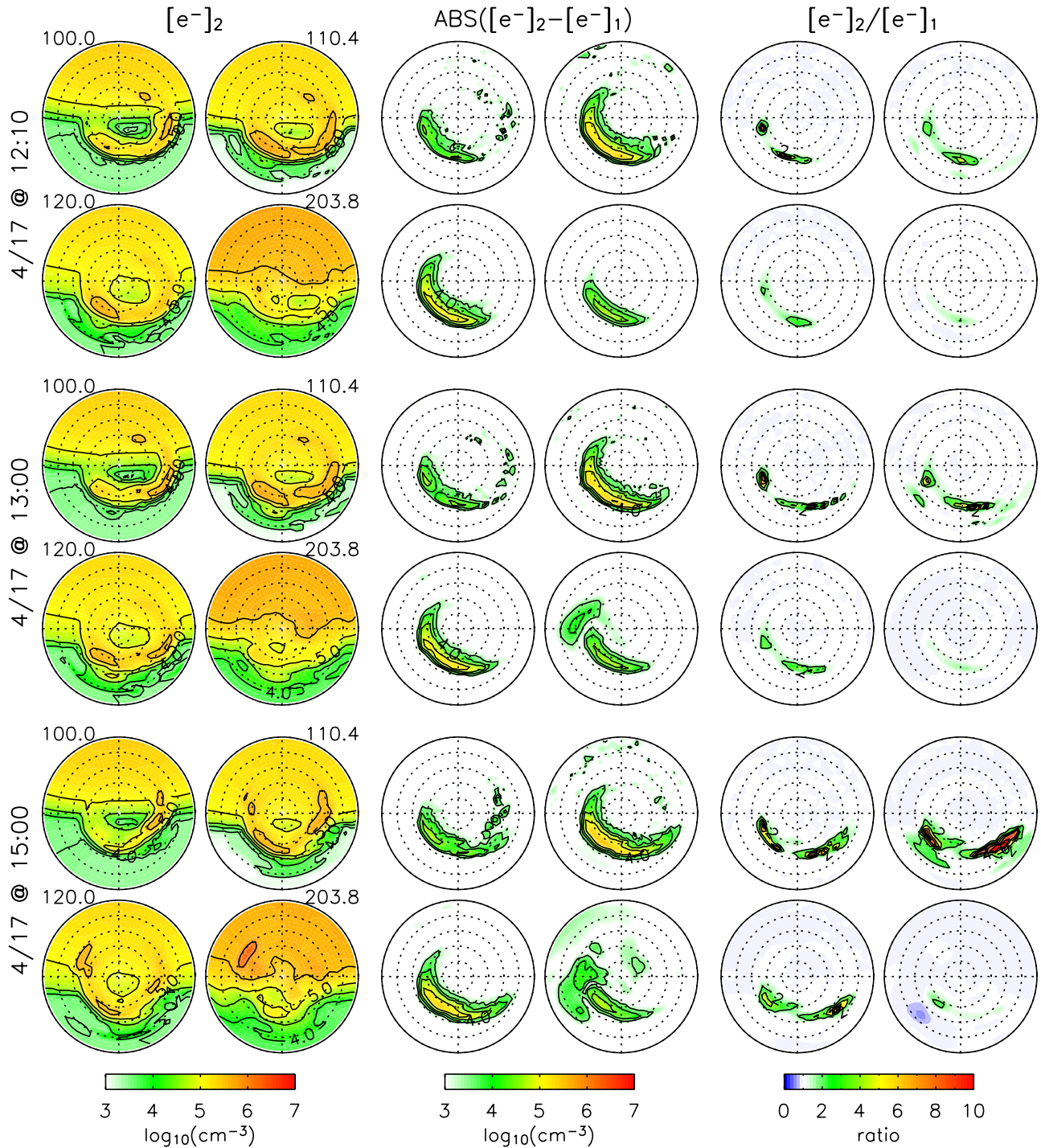
Figure 4. Comparison of ionospheric electron densitites in the absence (case one) or presence (case two) of proton precipitation. In the GITM simulation case two, a proton energy input is included starting from 1200 UT on 17 April 2002. The comparison is made at three times: (top two rows) 10 min later, (middle two rows) 1 hour later, and (bottom two rows) 3 hours later. The left two columns are for the electron concentration in the simulation case two. The middle two columns are for the absolute difference between case one and case two. The right two columns present the ratios of electron densities in the two cases. In each group of four dial plots, the simulation results are illustrated at different altitudes: (upper left) 100.0 km, (upper right) 110.4 km, (lower left) 120.0 km, and (lower right) 203.8 km.
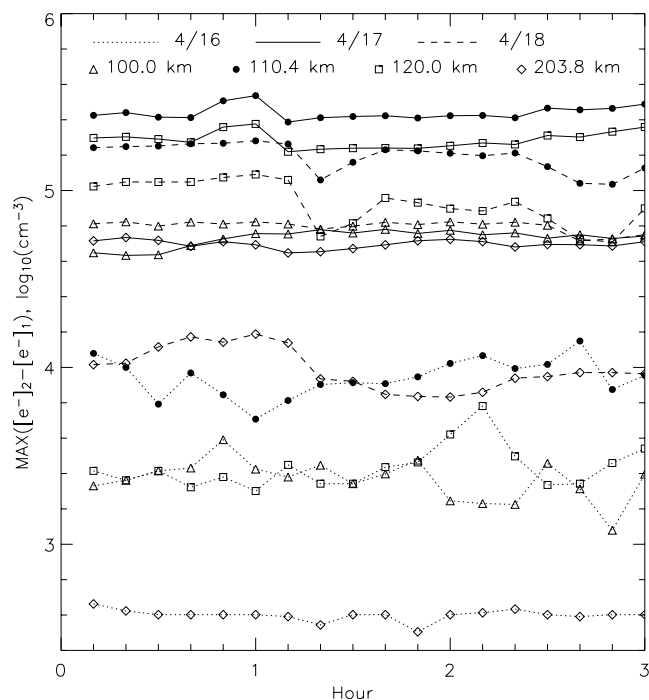
Figure 5. Temporal evolution of the maximum electron density enhancement due to the inclusion of a 3-hour proton precipitation starting from (1) 1200 UT on 16 April (dotted curves), (2) 1200 UT on 17 April (solid curves), or (3) 0300 UT on 18 April (dashed curves). The results are calculated at the altitudes of 100.0 km (triangle), 110.4 km (solid circle), 120.0 km (square), and 203.8 km (diamond). The data points are sampled every 10 min.

makes proton precipitation more focused in the evening sector. Second, proton ionization is negligible on the dayside, where the solar radiation dominates the ionosphere.

[30] Figure 4 has well illustrated how important it is to include global proton precipitation for correctly modeling the ionosphere. The calculation results indicate that there are significant enhancements in the magnitude of ionospheric electron densities after including precipitating protons, mostly in the evening sector at the equatorward edge of electron precipitation. As already seen in Figure 3, incident protons can also have a large effect on the thermosphere by changing the NO concentration. Similar to Figure 4, Figure 7 presents the change in the thermospheric NO densities at 10 min, 1 hour, and 3 hours after including proton precipitation in the GITM simulation. It is found that the proton impact on the thermosphere is almost entirely negligible under quiet time conditions (not shown here). During the storm, most of the proton effect on thermospheric NO is at low altitudes. Above ∼200 km, proton precipitation has a negligible effect on the NO abundance.

[31] The most noticeable feature in the time variation of the change in the NO density is the continuous buildup process. This is highlighted in Figure 8, which shows how the maximum enhancement in the NO density varies with time when precipitating protons are taken into account in the GITM simulation. In contrast with the temporal evolution of the enhancement in the ionospheric electron density (Figure 5), a clear increasing trend is observed in the

thermospheric nitric oxide increase as time goes on. The gradual increase is caused by the continuous proton precipitation and that NO has a long lifetime compared to the electrons. The effective life times of an NO molecule to chemical destruction under illuminated conditions and to diffusive transport are approximately 19 hours and 1 day, respectively [*Barth*, 1992; *Barth et al.*, 2001; *Bailey et al.*, 2002]. It is expected that if proton precipitation is continuously imposed for more than 1 day, as in the work of *Galand et al.* [1999], there should be no direct proportional relationship between the instantaneous intensities of proton precipitation and the resulting change in thermospheric NO densities. Rather, the NO abundance change will be associated with the integral effect of particle precipitation over the past 24 hours [e.g., *Bailey et al.*, 2002]. Also, owing to the long lifetime, the horizontal transport effect manifests itself in the temporal pattern change of the NO density enhancement produced by proton precipitation. As shown in
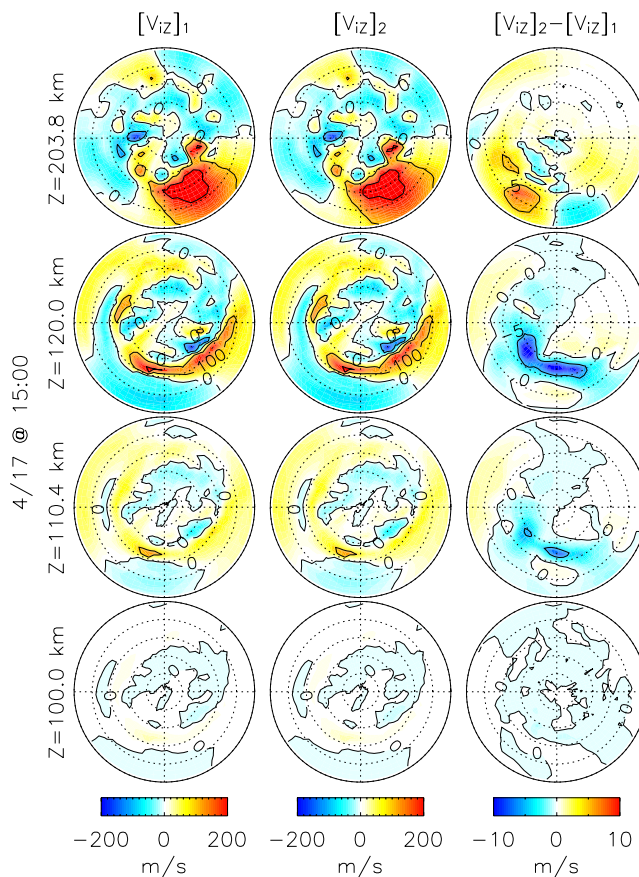

Figure 6. Comparison of vertical upward ion velocities between GITM simulations by excluding or including a 3-hour proton precipitation beginning at 1200 UT on 17 April 2002. The left column is the calculation results when only electron precipitation is considered. The middle column is the vertical velocity with the inclusion of proton precipitation in the simulation. The right column corresponds to the change due to the proton impact. The results are displayed at four altitudes: (top) 203.8 km, (second row) 120.0 km, (third row) 110.4 km, and (bottom) 100.0 km. Note that the contours are plotted on a linear scale.
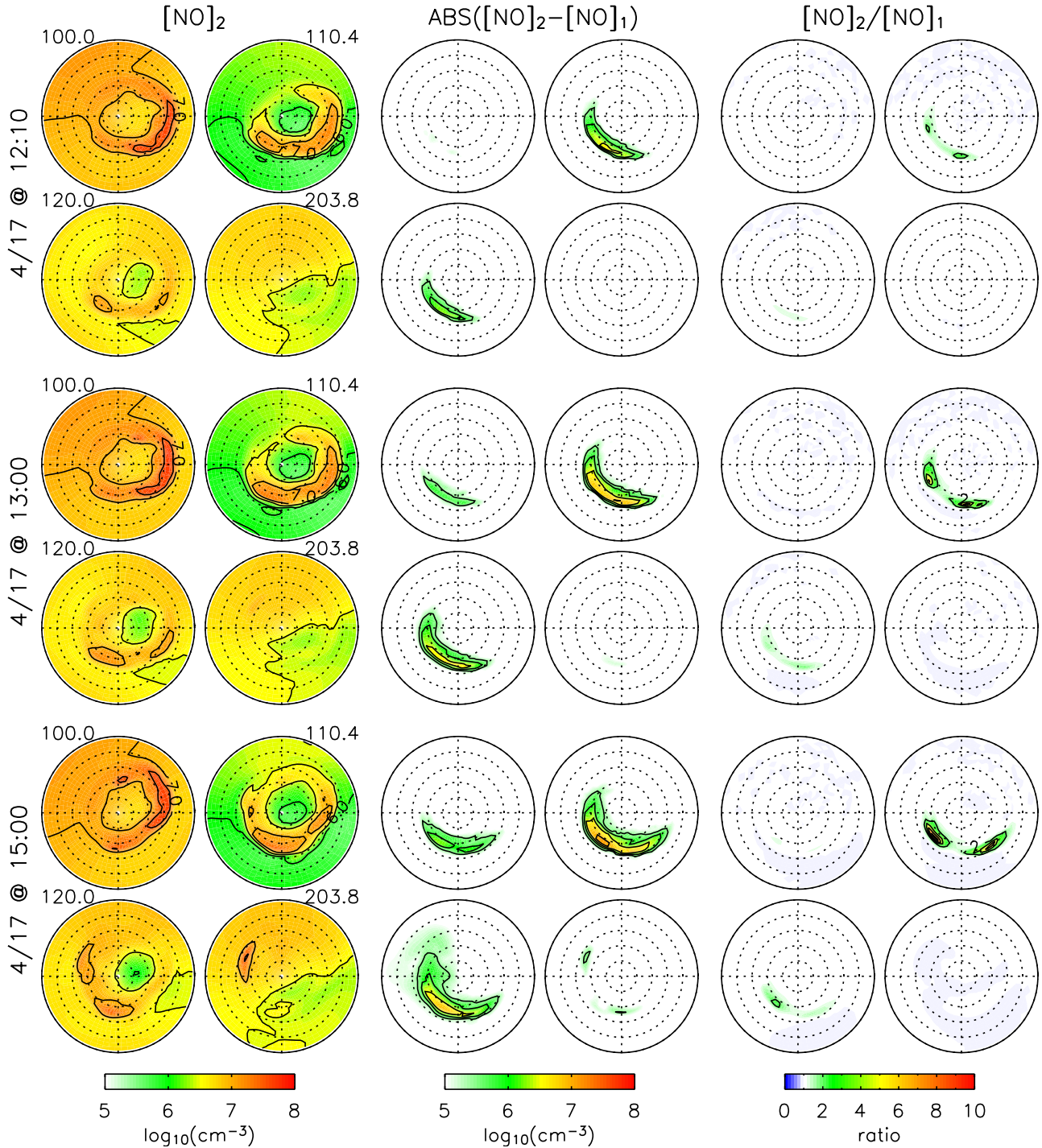
Figure 7. Similar to Figure 4 but for the comparison of thermospheric NO densitites.

Figure 7, the regions of large net increase expand during the 3-hour period, in both the longitudinal and latitudinal directions.

[32] As already illustrated in Figure 6, ion convection changes in response to proton precipitation. A detailed examination of the impact of proton precipitation on the ionospheric ion and thermospheric neutral convection is presented in Figure 9 and Figure 10, respectively. It is seen that the changes in the convection patterns take place in regions that are consistent with topside proton energy input.

In the selected sheath driven storm (17 April), extra proton precipitation in GITM has a significant effect on the convection: locally about ±20% change in ion velocities and about ±40% change in neutral winds. It is well known that with less neutrals or more ions, ions in the E region tend to $\mathbf{E} \times \mathbf{B}$ drift. In this case, proton precipitation results in an enhancement of electron densities and thus the ratios of ions and neutrals, allowing ion convection to be more aligned with $\mathbf{E} \times \mathbf{B}$ drift. These comparisons of the horizontal and vertical components of ion and neutral wind velocities
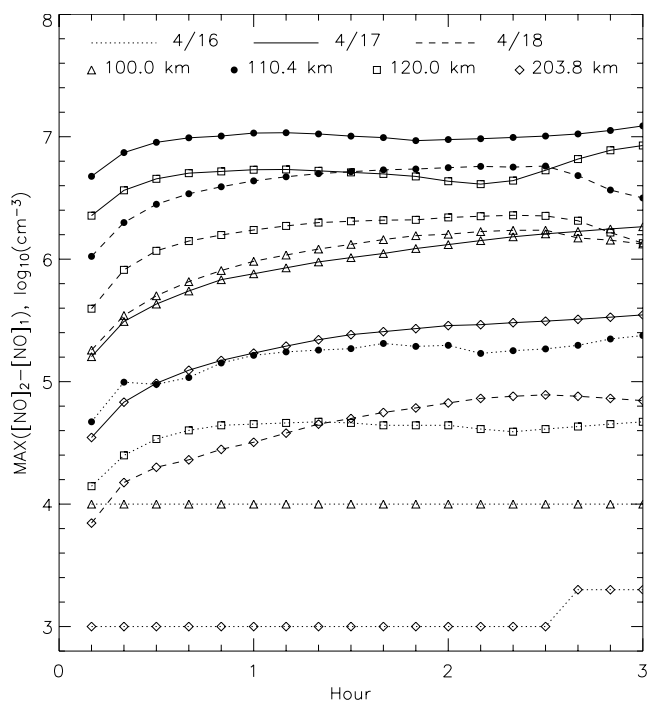
Figure 8. Similar to Figure 5 but for thermospheric NO densities.

highlight the ionosphere-thermosphere coupling process: incident protons produce conductivity changes (see paper 2) that drive disturbances in the ion convection, and ultimately affect the neutral dynamics through ion-neutral collisions.

4. Discussion

[33] The significance of including proton precipitation in a global ionosphere-thermosphere coupled model (like GITM) has been underscored by the direct influence on the electron and nitric oxide abundances. It is shown that even in a moderate geomagnetic storm (like April 2002), precipitating protons can make large contributions to the electron and nitric oxide density enhancements in the E region. At a higher level of magnetospheric activity (and thus having stronger proton precipitation), the role of incident protons in the ionosphere and thermosphere system is expected to become more important and thus certainly deserves to be included in a global model.

[34] As already emphasized in paper 2, the present study is concentrated on high-energy precipitating protons, that is, falling within the energy range of 30–240 keV. This energy band is representative of the bulk of ring current ions and plasma sheet ions in its high-energy tail. The inclusion of low-energy components (<30 keV) definitely will enhance the relative contribution of precipitating protons. This is an interesting topic for a future research study.

[35] It should be noted that secondary electrons produced in proton precipitation are not considered in the current version of the 3-D Monte Carlo ion transport model [*Fang et al.*, 2004]. That is, the further ionization and heating generated by secondary electrons are temporarily omitted from consideration and not fed into GITM. By taking this

secondary effect into account, we can expect larger changes in the ionosphere-thermosphere system. In other words, the results yielded in this paper represent a lower limit of the global proton impact. The addition of secondary electrons into the particle transport calculation is one of the important parts of the planned model improvement. A two-stream suprathermal electron transport model [e.g., *Nagy and Banks*, 1970] will be employed to calculate the distribution and effects of the secondary electrons. The other model developments include considering magnetic mirroring effect due to nonuniform magenetic fields as well as replacing the forward scattering approximation used for our current modeling of inelastic collisions with a more realistic treatment of collisional scattering.

5. Summary and Conclusion

[36] In paper 1, global 30–240 keV proton precipitation patterns during the 17–18 April 2002 storms are constructed at a 3-hour cadence using in situ NOAA/POES satellite measurements. The resulting ionization rates, and
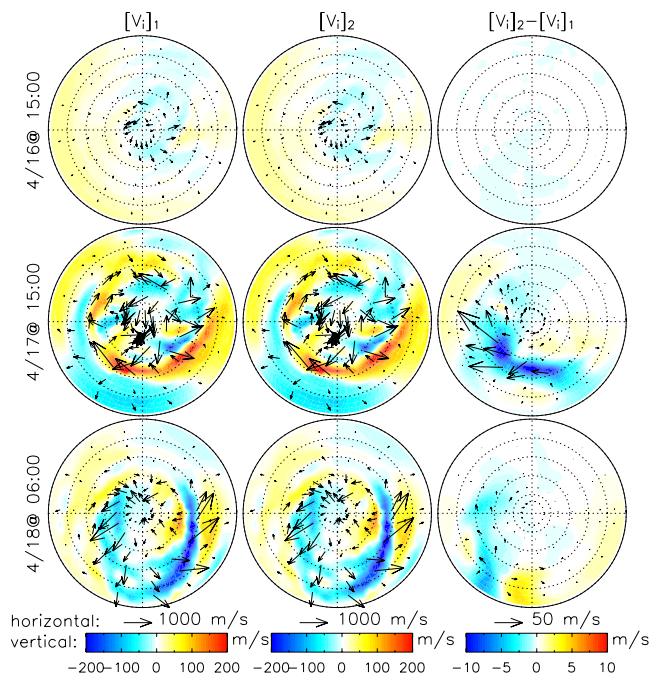

Figure 9. Comparison of ion velocity field at 120 km altitude between GITM simulations with the exclusion or inclusion of a 3-hour proton precipitation, which begins (top row) at 1200 UT on 16 April 2002, (middle row) at 1200 UT on 17 April 2002, or (bottom row) at 0300 UT on 18 April 2002. The arrows indicate horizontal ion convection velocity, superposed on the contour maps of vertical upward velocity components. The left column is for the simulation case one, when only electron precipitation is considered. The middle column corresponds to the simulation case two, when additional proton precipitation is included. The right column shows the change between the two cases. Note that the horizontal velocity scale bar and the vertical velocity color bar (shown at the bottom) for the right column are different from the others.
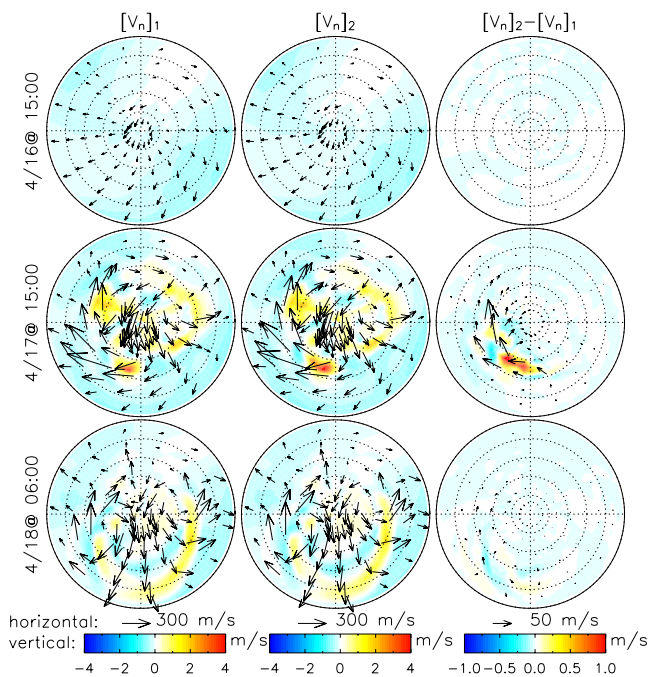
Figure 10. Similar to Figure 9 but for the comparison of neutral winds. Note that the vertical velocity components (color contours) are mass-weighted over all the neutral species.

therefore conductances, are assessed in paper 2 by running our 3-D Monte Carlo ion transport model [*Fang et al.*, 2004]. In this paper, the disturbances resulting from proton precipitation are coupled into the Global Ionosphere Thermosphere Model [*Ridley et al.*, 2004b, 2006] that is developed at the University of Michigan. For the first time, using in situ particle flux measurements, we can examine on a planetary scale the geoeffectiveness of storm time proton precipitation on the coupled ionosphere and thermosphere system.

[37] This work represents a similar study as those conducted by *Galand et al* [1999, 2001] but with some significant improvements. Rather than relying on the statistical particle precipitation models used in the studies of *Galand et al.* [1999, 2001], observational particle precipitation data during the April 2002 geomagnetic storms were used. These realistic particle precipitation conditions facilitate a more accurate quantitative assessment of the upper atmospheric geoeffectiveness. Moreover, for ion precipitation, the horizontal spreading effect is a unique feature due to charge exchange and electron stripping collisions within an incident beam [*Fang et al.*, 2004, 2005, and references therein]. It has been illustrated in the studies of *Fang et al.* [2004, 2005] and paper 2 that significant errors in the ionization rates and the Pedersen and Hall conductances are induced in association with the neglect of the beam spreading effect. The beam spreading is included in a natural way in this paper using our 3-D Monte Carlo ion transport model, while it cannot be modeled in 1-D calculations.

[38] By comparing the ionospheric and thermospheric states in the presence or absence of proton precipitation, it

is shown that after the addition of proton precipitation in a moderate geomagnetic storm like the one during April 2002, there are places at low altitudes (100–120 km) on the nightside undergoing significant enhancement (several times to an order of magnitude increase) in electron and nitric oxide densities. The study of the time variation shows that in general, the enhancement in ionospheric electron densities has a direct correlation with proton precipitation and there is no clear trend observed with time. On the contrary, a continuous buildup process is demonstrated for the temporal evolution of the thermospheric NO density enhancement when proton precipitation is added. This is because of the long lifetime of NO at these altitudes (around 19 hours). In addition, it is suggested that including observed high-energy precipitating protons in a global ionosphere thermosphere coupled model has a significant effect on the ion convection (locally around ±20% change) and on the neutral winds (locally around ±40%).

[39] This paper is focused on the impact of observed energetic proton precipitation on the ionosphere and thermosphere during the 17–18 April 2002 storms. The quantification of the changes when proton energy inputs are added into GITM evidently shows that precipitating protons take on a significant role in the ionosphere and thermosphere modeling. It implies that although most of the kinetic particle energy input generally comes from electrons with protons contributing around 15% [*Hardy et al.*, 1989; *Galand et al.*, 2001], the importance of proton precipitation to the coupled ionosphere and thermosphere system should not be ignored, especially during a high level of magnetospheric activity. It is still unknown to what extent proton precipitation, in turn, affects the near-Earth magnetosphere through the ionosphere-magnetosphere coupling.

References

André, M., and A. Yau (1997), Theories and observations of ion energization and outflow in the high latitude magnetosphere, *Space Sci. Rev.*, *80*, 27.

Bailey, S. M., C. A. Barth, and S. C. Solomon (2002), A model of nitric oxide in the lower thermosphere, *J. Geophys. Res.*, *107*(A8), 1205, doi:10.1029/2001JA000258.

Baker, D. N., C. A. Barth, K. E. Mankoff, S. G. Kanekal, S. M. Bailey, G. M. Mason, and J. E. Mazur (2001), Relationship between precipitating auroral zone electrons and lower thermospheric nitric oxide densities: 1998–2000, *J. Geophys. Res.*, *106*, 24,465.

Barth, C. A. (1992), Nitric oxide in the lower thermosphere, *Planet. Space Sci.*, *40*, 315.

Barth, C. A., S. M. Bailey, and S. C. Solomon (1999), Solar-terrestrial coupling: Solar soft X-rays and thermospheric nitric oxide, *Geophys. Res. Lett.*, *26*, 1251.

Barth, C. A., D. N. Baker, K. D. Mankoff, and S. M. Bailey (2001), The northern auroral region as observed in nitric oxide, *Geophys. Res. Lett.*, *28*, 1463.

Basu, B., J. R. Jasperse, R. M. Robinson, R. R. Vondrak, and D. S. Evans (1987), Linear transport theory of auroral proton precipitation: A comparison with observations, *J. Geophys. Res.*, *92*, 5920.

Bilitza, D. (2001), International Reference Ionosphere 2000, *Radio Sci.*, *36*, 261.

Callis, L. B., M. Natarajan, J. D. Lambeth, and D. N. Baker (1998), Solar atmospheric coupling by electrons (SOLACE), 2, Calculated stratospheric effects of precipitating electrons, 1979–1988, *J. Geophys. Res.*, *103*, 28,421.

Chappell, C. R., T. E. Moore, and J. H. Waite (1987), The ionosphere as a fully adequate source of plasma for the Earth's magnetospphere, *J. Geophys. Res.*, *92*, 5896.

Clauer, C. R., X. Cai, D. Welling, A. DeJong, and M. G. Henderson (2006), Characterizing the 18 April 2002 storm-time sawtooth events using ground magnetic data, *J. Geophys. Res.*, *111*, A04S90, doi:10.1029/2005JA011099.

Codrescu, M. V., T. J. Fuller-Rowell, R. G. Roble, and D. S. Evans (1997), Medium energy particle precipitation influences on the mesosphere and lower thermosphere, *J. Geophys. Res.*, *102*, 19,977.

Fang, X., M. W. Liemohn, J. U. Kozyra, and S. C. Solomon (2004), Quantification of the spreading effect of auroral proton precipitation, *J. Geophys. Res.*, *109*, A04309, doi:10.1029/2003JA010119.

Fang, X., M. W. Liemohn, J. U. Kozyra, and S. C. Solomon (2005), Study of the proton arc spreading effect on primary ionization rates, *J. Geophys. Res.*, *110*, A07302, doi:10.1029/2004JA010915.

Fang, X., M. W. Liemohn, J. U. Kozyra, D. S. Evans, A. D. DeJong, and B. A. Emery (2007a), Global 30–240 keV proton precipitation in the 17–18 April 2002 geomagnetic storms: 1. Patterns, *J. Geophys. Res.*, *112*, A05301, doi:10.1029/2006JA011867.

Fang, X., M. W. Liemohn, J. U. Kozyra, and D. S. Evans (2007b), Global 30–240 keV proton precipitation in the 17–18 April 2002 geomagnetic storms: 2. Conductances and beam spreading, *J. Geophys. Res.*, *112*, A05302, doi:10.1029/2006JA012113.

Frahm, R. A., J. D. Winningham, J. R. Sharber, R. Link, G. Crowley, E. E. Gaines, D. L. Chenette, B. J. Anderson, and T. A. Potemra (1997), The diffuse aurora: A significant source of ionization in the middle atmosphere, *J. Geophys. Res.*, *102*, 28,203.

Frey, H. U., S. B. Mende, C. W. Carlson, J.-C. Gérard, B. Hubert, J. Spann, R. Gladstone, and T. J. Immel (2001), The electron and proton aurora as seen by IMAGE-FUV and FAST, *Geophys. Res. Lett.*, *28*, 1135.

Fuller-Rowell, T. J., and D. S. Evans (1987), Height-integrated Pederson and Hall conductivity patterns inferred from the TIROS-NOAA satellite data, *J. Geophys. Res.*, *92*, 7606.

Fuller-Rowell, T. J., M. V. Codrescu, H. Rishbeth, R. J. Moffett, and S. Quegan (1996), On the Seasonal response of the thermosphere and the ionosphere to geomagnetic storms, *J. Geophys. Res.*, *101*, 2343.

Galand, M., R. G. Roble, and D. Lummerzheim (1999), Ionization by energetic protons in Thermosphere-Ionosphere Electrodynamics General Circulation Model, *J. Geophys. Res.*, *104*, 27,973.

Galand, M., T. J. Fuller-Rowell, and M. V. Codrescu (2001), Response of the upper atmosphere to auroral protons, *J. Geophys. Res.*, *106*, 127.

Gérard, J.-C., and C. A. Barth (1977), High-latitude nitric oxide in the lower thermosphere, *J. Geophys. Res.*, *82*, 674.

Gérard, J.-C., B. Hubert, M. Meurant, V. I. Shematovich, D. V. Bisikalo, H. Frey, S. B. Mende, G. R. Gladstone, and C. W. Carlson (2001), Observation of the proton aurora with IMAGE FUV imager and simultaneous ion flux in situ measurements, *J. Geophys. Res.*, *106*, 28,939.

Hardy, D. A., M. S. Gussenhoven, and E. Holeman (1985), A statistical model of auroral electron precipitation, *J. Geophys. Res.*, *90*, 4229.

Hardy, D. A., M. S. Gussenhoven, and R. Raistrick (1987), Statistical and functional representations of the pattern of auroral energy flux, number flux, and conductivity, *J. Geophys. Res.*, *92*, 12,275.

Hardy, D. A., M. S. Gussenhoven, and D. Brautigam (1989), A statistical model of auroral ion precipitation, *J. Geophys. Res.*, *94*, 370.

Hardy, D. A., W. McNeil, M. S. Gussenhoven, and D. Brautigam (1991), A statistical model of auroral ion precipitation: 2. Functional representation of the average patterns, *J. Geophys. Res.*, *96*, 5539.

Hedin, A. E. (1991), Extension of the miss thermosphere model into the middle and lower atmosphere, *J. Geophys. Res.*, *96*, 1159.

Henderson, M. G., G. D. Reeves, R. Skoug, M. T. Thomsen, M. H. Denton, S. B. Mende, T. J. Immel, P. C. Brandt, and H. J. Singer (2006), Magneto-spheric and auroral activity during the 18 April 2002 sawtooth event, *J. Geophys. Res.*, *111*, A01S90, doi:10.1029/2005JA011111.

Liemohn, M. W., A. J. Ridley, D. L. Gallagher, D. M. Ober, and J. U. Kozyra (2004), Dependence of plasmaspheric morphology on the electric field description during the recovery phase of the 17 April 2002 magnetic storm, *J. Geophys. Res.*, *109*, A03209, doi:10.1029/2003JA010304.

Liemohn, M. W., A. J. Ridley, P. C. Brandt, D. L. Gallagher, J. U. Kozyra, D. M. Ober, D. G. Mitchell, E. C. Roelof, and R. DeMajistre (2005), Parametric analysis of nightside conductance effects on inner magneto-spheric dynamics for the 17 April 2002 storm, *J. Geophys. Res.*, *110*, A12S22, doi:10.1029/2005JA011109.

Lyons, L. R., and D. S. Evans (1984), An association between discrete aurora and energetic particle boundaries, *J. Geophys. Res.*, *89*, 2395.

Mende, S. B., et al. (2000), Far ultraviolet imaging from the IMAGE space-craft. 1. System design, *Space Sci. Rev.*, *91*, 243.

Nagy, A. F., and P. M. Banks (1970), Photoelectron fluxes in the ionosphere, *J. Geophys. Res.*, *75*, 6260.

Rawer, K., D. Bilitza, and S. Ramakrishnan (1978), Goals and status of the International Reference Ionosephre, *Rev. Geophys.*, *16*, 177.

Richmond, A. D. (1992), Assimilative mapping of ionospheric electrodynamics, *Adv. Space Res.*, *12*, 59.

Richmond, A. D., and Y. Kamide (1988), Mapping electrodynamics features of the high-latitude ionosphere from localized observations: Technique, *J. Geophys. Res.*, *93*, 5741.

Ridley, A. J., T. I. Gombosi, and D. L. DeZeeuw (2004a), Ionospheric control of the magnetosphere: conductance, *Ann. Geophys.*, *22*, 567.

Ridley, A. J., G. Tóth, Y. Deng, J. Kozyra, T. Immel, and L. Paxton (2004b), The Global Ionosphere Thermosphere Model results of the April 2002 storm, *Eos Trans. AGU*, *85*(17), Jt. Assem. Suppl., Abstract SA1A-07.

Ridley, A. J., Y. Deng, and G. Tóth (2006), The global ionosphere-thermosphere model, *J. Atmos. Sol. Terr. Phys.*, *68*, 839.

Roble, R. G. (1992), The polar lower thermosphere, *Planet. Space Sci.*, *40*, 271.

Roble, R. G., and E. C. Ridley (1987), An auroral model for the NCAR thermospheric general circulation model (TGCM), *Ann. Geophys.*, *5*, 369.

Senior, C., J. R. Sharber, O. De La Beaujardière, R. A. Heelis, D. S. Evans, J. D. Winningham, M. Sugiura, and W. R. Hoegy (1987), E and F region study of the evening sector auroral oval: A Chatanika/Dynamics Explorer 2/NOAA 6 comparison, *J. Geophys. Res.*, *92*, 2477.

Siskind, D. E., C. A. Barth, D. S. Evans, and R. G. Roble (1989), The response of thermospheric nitric oxide to an auroral storm: 2. Auroral latitudes, *J. Geophys. Res.*, *94*, 16,899.

Smirnova, N. V., A. N. Lyakhov, Y. I. Setzer, A. P. Osepian, C. I. Meng, R. Smith, and H. C. Stenbaek-Nielsen (2004), Precipitating protons and their role in ionization of the polar ionosphere, *Cosmic Res.*, *42*, 210.

Taylor, F. W. (1991), The greenhouse effect and climate change, *Rep. Progr. Phys.*, *54*, 881.

Weimer, D. (1996), A flexible, IMF dependent model of high-latitude electric potentials having "space weather" applications, *Geophys. Res. Lett.*, *23*, 2549.

————————————

X. Fang, J. U. Kozyra, M. W. Liemohn, and A. J. Ridley, Space Physics Research Laboratory, University of Michigan, 2455 Hayward Street, Ann Arbor, MI 48109-2143, USA. (xhfang@umich.edu; jukozyra@umich.edu; liemohn@umich.edu; ridley@umich.edu)

D. S. Evans, Space Environment Center, National Oceanic and Atmospheric Administration, 325 Broadway, Boulder, CO 80303, USA. (david.s.evans@noaa.gov)